KRONOS FUSION ENERGY

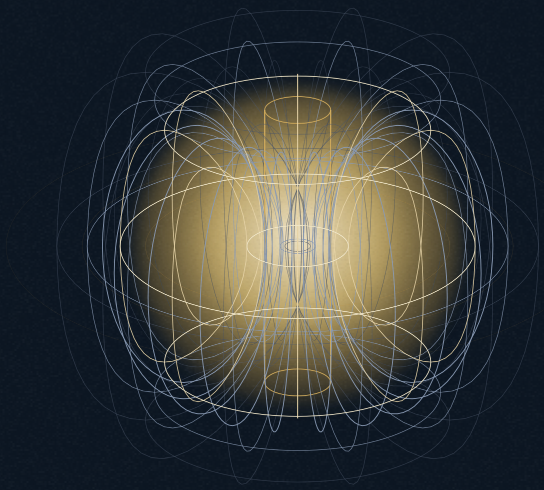

PAPER 2.37 · THE KRONOS 2026 SERIES

A Stacked Detachment Portfolio for a Compact Spherical-Tokamak Breeder: Super-X, Double-Null and Snowflake Geometries that Cut the Required Argon Seed Fraction

Exhausting the power that crosses the separatrix without melting the target is the binding engineering risk of a compact, high-power-density spherical-tokamak (ST) breeder: the...

Read it live — 3-D model · physics validator · film series

BY P I FORD AND G L KULCINSKI

2026 · EDITORIAL EDITION

THE OFFICIAL RECORD

What this document is, and how to read its numbers

This is a combined editorial. It gathers, in one volume, the two design studies Kronos Fusion Energy released in 2026 — a compact spherical-tokamak tritium/helium-3 breeder and a deuterium–helium-3 tandem-mirror generator — together with the intellectual-property estate, the people, and, in the internal edition, the full commercial case. The scientific text is the same text that appears in the arXiv preprints and the journal submissions; the editorial adds the apparatus a reader needs to hold the whole program at once, and nothing in the physics is altered to fit it.

THE HONESTY STANCE IS THE ASSET

Every headline quantity carries an **evidence class** — DERIVED RECOMPUTED MEASURED REQUIREMENT — and, where a number is a modelled extrapolation rather than a demonstrated value, it is labelled as such and its downside is shown next to it. Several quantities in the underlying corpus moved after first publication; where a value has been withdrawn or restated, the record says so plainly. This is deliberate: a diligence team will find the load-bearing assumptions, so the document surfaces them first.

TWO EDITIONS

This volume is issued in two editions. The **public edition** (light) carries the physics and the design only — no dollar, price, or per-kilogram figure appears anywhere in it. The **internal edition** (dark) adds the economics, the funding architecture, and the defense-commercial analysis, and is marked *Confidential* accordingly; it is not for public distribution. Where the commercial case rests on a modelled assumption rather than a demonstrated one, it is labelled as such and its downside is shown alongside it, on the same terms as the physics.

TITLE	The Kronos Fleet — Hyperion · Aegis · MetroVolt: A Combined Design & Commercialization Study
AUTHOR	Priyanca Ford, Founder & CEO, on behalf of Kronos Fusion Energy
EDITION	2026 Combined Editorial · first issue
COMPANION WORKS	The five-paper arXiv drop — (1) Breeder, (2) Burner, (3) REBCO magnet & tape, (4) Direct Energy Conversion, (5) AI/ML/Quantum control — with matching numbered Zenodo deposits, plus the IOP journal and IAEA-FEC submissions. Patents were filed before the drop.
NAMING	Hyperion = the breeder; Aegis (defense) and MetroVolt (data-center) = one generator in two housings. Internal mode letters (D1, L) do not appear on public surfaces.
STATUS	Conceptual design & simulation study. Nothing herein is a construction commitment.

HOW TO READ THIS VOLUME

The fleet at a glance, and the way its numbers are marked

This volume opens with *Orientation*, presents the five research papers as a bound sequence, and closes with the *Apparatus*. *Foundations* sets out the three general results both machines rest on. *Paper One* is the Hyperion breeder; *Paper Two* the Aegis / MetroVolt generator; *Papers Three, Four and Five* are the enabling science — high-field REBCO magnets and tape, direct energy conversion, and the AI / ML / quantum control stack. A *Digital Twin & 3-D Model* part follows, then the *Environmental* profile. The *Economics* and levelized cost and the *Business Case* and diligence record appear in the internal edition only; the *Simulations* proof record and the Apparatus — patent portfolio, team, limitations, and sources — close both editions.

THE FLEET AT A GLANCE

	HYPERION	AEGIS	METROVOLT
Role	Strategic-isotope foundry	Defense installation power	Campus power
Machine	**Spherical tokamak**	**Tandem mirror**	**Tandem mirror**
Fuel	Deuterium–tritium	Deuterium–helium-3	Deuterium–helium-3
Delivers	Tritium · ^{3}He · 14 MeV n	Resilient installation power	Firm campus power
Physics bar	**Fusion gain only**	Closure (gates named)	Closure + lunar ^{3}He
In the fleet	Breeds the fuel	Proves the generator	Commercial destination

HOW THE NUMBERS ARE MARKED

Every headline quantity carries an evidence class — DERIVED from first principles, RECOMPUTED from raw data, MEASURED in hardware, or a REQUIREMENT yet to be met. Financial figures carry a case label and are confined to the internal (confidential) edition. Values that moved after first publication are shown as withdrawn or restated rather than quietly changed. A capability you can evaluate is one whose limits are on the page.

ABSTRACT

A Stacked Detachment Portfolio for a Compact Spherical-Tokamak Breeder: Super-X, Double-Null and Snowflake Geometries that Cut the Required Argon Seed Fraction

Exhausting the power that crosses the separatrix without melting the target is the binding engineering risk of a compact, high-power-density spherical-tokamak (ST) breeder: the machine is small, the parallel heat flux is large, and the scrape-off-layer (SOL) channel is narrow. For the Hyperion breeder design point ($I_p = 9.66\,MA$, $Q = 3.076$, $P_{\text{fus}} = 85.04\,MW$, $\delta = -0.30$, $B_0 = 8\,T$, $\kappa = 2.0$, $R_0 = 1.20\,m$, aspect ratio $A = 2.5$) the design-basis heat-flux width is $\lambda_q \approx 0.337\,mm$ and the parallel heat flux $q_{\|} \approx 12\,GW/m^2$; a conventional single-null divertor would demand an argon seed fraction near $6.4\,\%$ to detach, several times the tolerable level for core contamination. We treat the divertor as a *requirement* closed by a bounded portfolio, not as a solved number. We derive the reduced-order chain that sets the requirement — the Eich/Goldston width scaling, the conduction-limited two-point model, and the Lengyel impurity-radiation integral — and show analytically how three geometric power-spreading levers compose: a Super-X long-leg divertor increases the target major radius and connection length, a double null splits the exhaust over two strike points, and a snowflake-like second-order null adds poloidal flux expansion. One-dimensional screening walks the required argon seed down a ladder $6.4\% \rightarrow 2\text{--}3\%$ (Super-X) $\rightarrow\approx 1\%$ (Super-X×double null) $\rightarrow\approx 0.5\%$ (Super-X×double null×snowflake), a tolerable seed, with the double-null power split (target flux $8.0 \rightarrow 4.4\,MW/m^2$, $1.8\times$) the dominant lever. A 4000-sample Monte-Carlo propagation of the input uncertainties returns a closure probability at $c_{\text{Ar}} \leq 0.5\%$ of 0% for Super-X alone, 52% for Super-X×double-null, and 95% for the full stack. Four independent one-dimensional edge codes (SD1D/Hermes-3 on BOUT++, UEDGE, a self-written parallel solver, and the analytic Lengyel model) agree that seeding is mandatory and that a sub-one-percent seed detaches. The honest status is that the decisive two-dimensional edge-transport calculation (SOLPS-ITER, B2.5–EIRENE) was blocked by the absence of a divertor-legged equilibrium; a free-boundary Super-X null with a genuine X-point has now been constructed, which unblocks it, and we credit no two-dimensional detachment number we did not compute. All quantitative claims are grounded in the frozen Kronos Physics De-Risking Register and were produced on the NVIDIA GPU HPC campaign.

Open-access deposit (code & data, CC BY 4.0): DOI 10.5281/zenodo.22645742 · Zenodo community *kronos_fusion_energy*. Explore it live: interactive 3-D model · physics validator.

Keywords: divertor detachment Super-X double null snowflake divertor scrape-off layer impurity seeding heat exhaust SOLPS-ITER spherical-tokamak breeder

CONTENTS

Table of Contents

NOMENCLATURE

Symbols, units, and the names of things

Q	plasma (fusion) gain, P_{fus}/P_{aux}
Q_E	engineering gain, net electric out / recirculating in
H_{98}	confinement enhancement over the IPB98(y,2) scaling
Z_{eff}	effective ion charge
c_{ee}	electron–electron bremsstrahlung leading coefficient, 2.120022 (exact)
τ_E	energy confinement time
I_p	plasma current
R_0, a	major radius, minor radius
κ, δ	elongation, triangularity
β_N	normalized plasma beta (Troyon-normalized)
TBR	tritium breeding ratio
DEC	direct energy conversion
CF	plant capacity factor (availability)
FOAK / NOAK / BOAK	first / n^{th} / best of a kind
Hyperion	the ST breeder (internal: Mode D2)
Aegis	the generator, defense/installation housing (internal: Mode M)
MetroVolt	the generator, data-center housing (Mode M)

§ 1

Introduction

THE EXHAUST PROBLEM OF A COMPACT BREEDER

A spherical tokamak confines a large plasma current in a small volume, which is exactly what makes it an attractive compact neutron source and tritium/helium-3 breeder platform [1,2] and, at the same time, what makes the power-exhaust problem acute. The Hyperion breeder holds $I_p = 9.66\,MA$ at a major radius of only $R_0 = 1.20\,m$ behind a centrepost magnet at a peak field of $16.84\,T$, in a negative-triangularity ($\delta = -0.30$) regime chosen for confinement without an edge pedestal and its edge-localised-mode (ELM) cycle [3,4]. The power that leaves the confined plasma is funnelled into a scrape-off layer (SOL) whose width, in high-field compact devices, is a fraction of a millimetre; the resulting parallel heat flux is an order of magnitude above any bare-material limit. This is the same challenge that reactor-class compact tokamaks confront quantitatively — for SPARC, Kuang *et al.* project a peak unmitigated parallel heat flux "greater than $10\,GW/m^2$," nearly an order of magnitude above what has been demonstrated [5] — and it is the exhaust challenge, not the core physics, that most sharply distinguishes a compact high-power-density device from a large, low-power-density one [6,7].

DETACHMENT AND THE IMPURITY-SEED COST

The established route to a tolerable target load is *detachment*: dissipate the parallel power in line radiation, charge exchange and volumetric recombination before it reaches the plate, so that the target electron temperature falls to a few electron-volts and the plasma pressure — and thus the particle and heat flux — collapses in front of the surface [8,9]. Detachment is usually achieved by seeding a radiating impurity (nitrogen, neon or argon) [12,6]. But the seed is not free: impurities that radiate in the divertor also penetrate the core, dilute the fuel and radiate from the confined plasma, so the tolerable seed fraction is bounded from above. For the compact breeder, a single-null divertor requires a seed near $6.4\,\%$ argon to detach — several times a tolerable level. The exhaust problem is therefore not "can we detach" but "can we detach at a seed the core can survive."

ADVANCED DIVERTOR GEOMETRIES

The community's answer has been geometry. Three families of "advanced" magnetic divertor spread the power before it reaches the target, and each reduces the radiated fraction — and hence the seed — needed to detach. The *Super-X* divertor routes the outer leg to a large strike-point major radius, exploiting the $1/R$ fall of the toroidal field to expand the flux tube and lengthen the connection length [15,19]; on MAST Upgrade this produced a factor-~ 10 reduction in outer-target power load relative to a conventional divertor and a demonstrably wider detachment window [20,21]. The *snowflake* divertor places a second-order poloidal-field null near the primary X-point, where B_θ vanishes quadratically rather than linearly, strongly increasing poloidal flux expansion and the plasma-wetted area [16,17,18]. The *double null* splits the exhaust between two divertors. In a spherical tokamak these benefits are amplified, because the toroidal field falls most steeply with radius; the Super-X is predicted to be strongest exactly here.

CONTRIBUTION

What is missing for a specific compact ST breeder is a quantitative, honest account of *how far the geometry gets us* against a hard, frozen requirement, and of *what is still owed*. This paper provides that. Our contributions are: (i) a closed reduced-order derivation of the exhaust requirement from the width scaling through the two-point model to the Lengyel seed integral (§2); (ii) an analytic composition rule for the three geometric levers, yielding the argon-seed ladder $6.4\% \to 0.5\%$ (§3); (iii) a 4000-sample Monte-Carlo propagation that converts the ladder into a closure *probability* for each configuration (§3); (iv) a four-code cross-verification of the one-dimensional result (SD1D/Hermes-3, UEDGE, Lengyel, and a self-written parallel solver) that establishes seeding as mandatory and the seed as sub-one-percent (§5); (v) a description of the GPU-accelerated codes that produced these results and of the two-dimensional SOLPS-ITER calculation that remains the gating next step (§4, §6). Every headline quantity traces to a frozen serial in the Kronos Physics De-Risking Register [30]; the serial identifiers (e.g. BR-SX-09) are given inline so each number is auditable. The result narrows the divertor from "impossible" to "hard but bounded," and we are explicit throughout about what is a screening bound and what remains a target.

§ 2

Governing equations and the formal exhaust requirement

FROM SEPARATRIX POWER TO THE PARALLEL HEAT FLUX

Power crossing the separatrix, P_{SOL}, is set by the core turbulent transport that the negative-triangularity regime is chosen to suppress, computed for the design point by nonlinear gyrokinetics [28]; it flows into a SOL of characteristic e-folding width λ_q measured at the outer midplane. The parallel heat flux entering the divertor flux tube is

$$q_{\parallel} = \frac{P_{\mathrm{SOL}}}{2\pi R_0\,\lambda_q}\,\frac{B}{B_\theta},$$

where B/B_θ is the local total-to-poloidal field ratio that sets the field-line pitch. The narrowness of λ_q is set by edge physics. The Eich multi-machine regression gives a heat-flux width that scales inversely with the poloidal field, $\lambda_q\,[\mathrm{mm}] \approx 0.63\,B_\theta^{-1.19}$ [10], while the Goldston heuristic-drift model predicts $\lambda_q \sim 2a\rho_p/R_0$ from the ion magnetic drift across the separatrix into the SOL [11]; both collapse onto a sub-millimetre width at the high poloidal field of a compact high-current ST. For the frozen design point the negative-triangularity edge analysis returns $\lambda_q \approx 0.337\,mm$ (companion [31]), and equation (1) then gives $q_{\parallel} \approx 12\,GW/m^2$. Table 1 collects the design point and the derived SOL boundary condition; figure 6 shows the width and parallel-flux sensitivity across the Eich band, the Goldston estimate and a conservative reduced two-point solve.

QUANTITY	SYMBOL	VALUE	BASIS
plasma current	I_p	9.66 MA	canonical anchor
fusion power	P_{fus}	85.04 MW	canonical anchor
fusion gain	Q	3.076	canonical anchor
major radius	R_0	1.20 m	canonical anchor
aspect ratio	A	2.5	canonical anchor
elongation / triangularity	$\kappa,\ \delta$	$2.0,\ -0.30$	canonical anchor
on-axis / centrepost field	$B_0,\ B_{\mathrm{cp}}$	8 T, 16.84 T	canonical anchor
heat-flux width (design)	λ_q	0.337 mm	NT edge [31]
heat-flux width (conservative)	λ_q	0.21 mm	reduced 2PM, HX-14
parallel heat flux (design)	$q_{\parallel}$	12 GW/m^2	eq. (1)
target engineering limit	q_{lim}	$\approx 10\,MW/m^2$	CuCrZr, BV-06

Frozen design point (Tier-2 canonical anchors) and the derived scrape-off-layer boundary condition used throughout. Two heat-flux-width estimates bracket the design; the more conservative one strengthens the case for the stacked geometry (§5). Serials refer to the register [30].

THE TWO-POINT MODEL AND THE TARGET STATE

Along a divertor flux tube of connection length L, the parallel electron heat transport is Spitzer–H\"arm conduction-limited,

[redacted]

which integrates, for a spatially uniform upstream heat flux, to the conduction relation between the upstream and target electron temperatures T_u, T_t of the two-point model [9],

$$T_u^{7/2} = T_t^{7/2} + \frac{7}{2}\,\frac{q_{\parallel}\,L}{\kappa_{0e}}.$$

Static pressure balance along the field line, modified by a momentum-loss factor $f_{\mathrm{mom}} \in [0,1]$ that folds in charge-exchange and recombination friction, closes the model,

$$2\,n_t T_t = (1 - f_{\mathrm{mom}})\,n_u T_u,$$

and the target heat flux transmitted through the sheath is

$$q_t = \gamma\,n_t\,c_{s,t}\,T_t, \qquad c_{s,t} = \sqrt{\frac{2T_t}{m_i}},$$

with sheath transmission coefficient $\gamma \approx 7$–8. Equations (3)–(5) show the essential nonlinearity: as volumetric losses grow, T_t falls, the target pressure $n_t T_t$ collapses through equation (4), and q_t drops faster than linearly. Detachment is conventionally taken to begin when T_t falls below $\approx 5\,eV$, where volumetric recombination becomes significant. The projected target heat flux, before detachment, is

$$q_{\mathrm{target}} = (1 - f_{\mathrm{rad}})\,q_{\parallel}\,\sin\alpha,$$

with f_{rad} the radiated power fraction and α the field-line grazing angle at the plate. For the frozen design the unmitigated attached target flux, computed from equation (6) with a reduced two-point solve, is $\approx 1370\,MW/m^2$ for a conventional single-null geometry and $\approx 171\,MW/m^2$ for a Super-X leg (serial HX-14) — both far above the $\approx 10\,MW/m^2$ engineering ceiling of a water-cooled CuCrZr target (serial BV-06). Reaching the ceiling requires $f_{\mathrm{rad}} \gtrsim 0.94$ (detachment onset at $T_t \leq 5\,eV$ near $f_{\mathrm{rad}} \approx 0.91$); figure 3 plots the target-temperature descent, and figure 2 the target-flux reduction, of this chain.

THE LENGYEL SEED INTEGRAL

The radiated fraction must be supplied by a seeded impurity. In the Lengyel picture [13,12] an impurity of fractional concentration c_z radiating with cooling function $L_z(T)$ removes parallel heat flux over the temperature interval it spans, giving the closed relation between the upstream and target parallel fluxes,

$$q_{\parallel}^2(T_u) - q_t^2(T_t) = 2\,\kappa_{0e}\,c_z\,\big(n_e T_e\big)^2 \int_{T_t}^{T_u} L_z(T)\,\sqrt{T}\,\mathrm{d}T,$$

where $n_e T_e$ is (approximately) conserved along the tube. Solving equation (7) for the concentration required to drive q_t to the engineering ceiling,

$$c_z^{\mathrm{req}} = \frac{q_{\parallel}^2 - q_{\mathrm{lim}}^2}{2\,\kappa_{0e}\,(n_e T_e)^2 \displaystyle\int_{T_t}^{T_u} L_z(T)\sqrt{T}\,\mathrm{d}T},$$

exposes the two levers that reduce the seed: raising the radiative integral (choice of radiator; argon's L_z peaks in the divertor temperature range) and, crucially, *lowering the parallel flux $q_{\parallel}$ that arrives at the target*. The numerator scales as $q_{\parallel}^2$, so any geometric factor that reduces the target-directed parallel flux by a factor g reduces the required seed by nearly g^2 at fixed radiator. This quadratic sensitivity is the mathematical engine of the portfolio: geometry is a more powerful lever on the seed than radiator chemistry. Evaluating equation (8) at the design point with argon returns $c_{\mathrm{Ar}}^{\mathrm{req}} \approx 6.4\,\%$ for a conventional single null (figure 3).

GEOMETRIC FLUX SPREADING AS THE SEED LEVER

Three geometric operations reduce the effective target-directed $q_{\parallel}$ in equation (8). Define the *total flux expansion* of a divertor leg as

$$f_x = \frac{R_t\,B_{\theta,u}}{R_u\,B_{\theta,t}},$$

the product of a toroidal (major-radius) expansion R_t/R_u and a poloidal expansion $B_{\theta,u}/B_{\theta,t}$. A *Super-X* leg increases R_t (the strike-point major radius) and, in an ST where $B \propto 1/R$, simultaneously lowers the local field and lengthens the connection length L in equation (3); together these spread the strike-point flux by a factor ≈ 8 at a modest vessel extension. A *snowflake* places a second-order null where B_θ vanishes quadratically with distance r from the null, $B_\theta \propto r^2$ rather than $B_\theta \propto r$, so the poloidal flux expansion $B_{\theta,u}/B_{\theta,t}$ in equation (9) grows sharply near the target and the wetted area increases [16]. A *double null* does not expand a single leg; instead it *splits* P_{SOL} between two divertors, halving the per-target flux in equation (1). Writing the composed target-flux reduction as

$$g_{\mathrm{stack}} = g_{\mathrm{SX}} \cdot g_{\mathrm{DN}} \cdot g_{\mathrm{SF}},$$

and substituting $q_\parallel \to q_\parallel / g_{\text{stack}}$ into equation (8), the required seed falls as $c_z^{\text{req}} \propto g_{\text{stack}}^{-2}$ (for $q_\parallel \gg q_{\text{lim}}$). The three levers therefore *compose multiplicatively in flux and quadratically in seed*, which is the formal statement of the portfolio.

§ 3

The stacked-detachment portfolio

THE ARGON-SEED LADDER

Table 2 and figure 1 give the one-dimensional screening result: the argon seed fraction required to detach as the geometric levers of equation (10) are stacked (serial BR-L2-A11-SUM). A Super-X long-leg divertor alone lands near $2\text{–}3\,\%$; adding a double null roughly halves it to $\approx 1\%$, with the power split the dominant lever (steady target flux $8.0 \to 4.4\,MW/m^2$, a factor 1.8, serial BR-CX-02, figure 7); and adding a snowflake-like second-order null reaches $\approx 0.5\%$ — a tolerable seed. The geometric gain of the stack is order-ten spreading at a small radial cost, consistent with the $\sim 10\times$ outer-target reduction measured on MAST Upgrade for the Super-X alone [20].

DIVERTOR CONFIGURATION	REQUIRED AR SEED	FLUX SPREADING g_{stack}	$P(c_{\mathrm{Ar}} \leq 0.5\%)$
conventional single null	$\approx 6.4\%$	$1\times$	—
Super-X (long leg)	$\approx 2\text{–}3\%$	$\approx 8\times$	0%
Super-X $\times$ double null	$\approx 1\%$	$\approx 14\times$	52%
Super-X $\times$ double null $\times$ snowflake	$\approx 0.5\%$ (tolerable)	$\approx 18\text{–}20\times$	95%

Impurity-seed fraction required to detach as geometric power-spreading levers are stacked (one-dimensional Lengyel screening, serial BR-L2-A11-SUM). The chain narrows the requirement from several percent to a tolerable $\approx 0.5\%$. Flux-expansion factors are the composed g_{stack} of equation (10); the Monte-Carlo closure probability (serial BR-SX-09, $N = 4000$) is the probability that $c_{\mathrm{Ar}} \leq 0.5\%$ once input uncertainties are propagated.

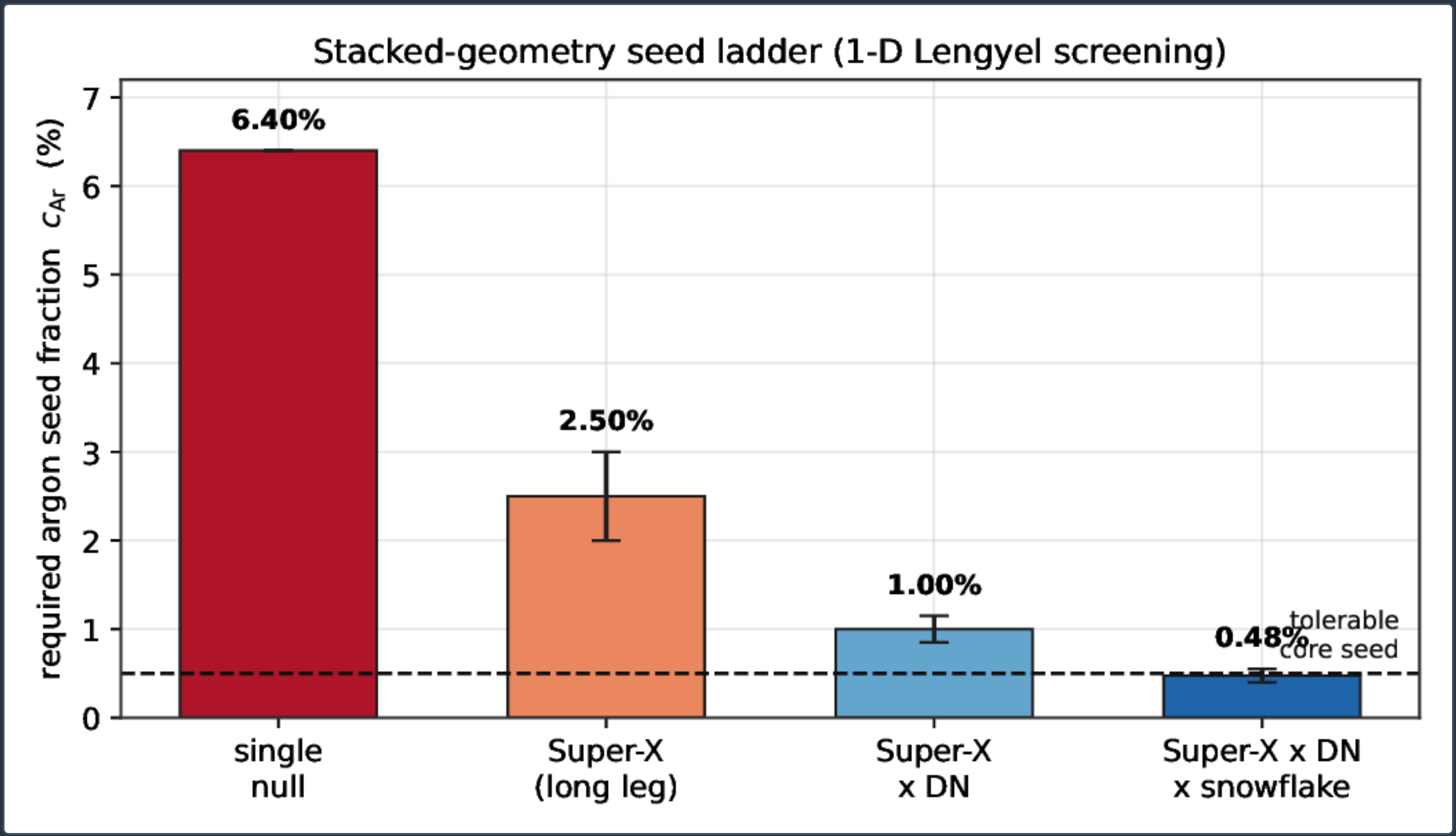

The argon-seed ladder (one-dimensional Lengyel screening, BR-L2-A11-SUM). As Super-X, double-null and snowflake levers are stacked, the argon seed fraction required to detach falls from $\approx 6.4\%$ (single null) to a tolerable $\approx 0.5\%$. Bars show the mid-band; whiskers the screening band. Dashed line marks the tolerable core-seed level.

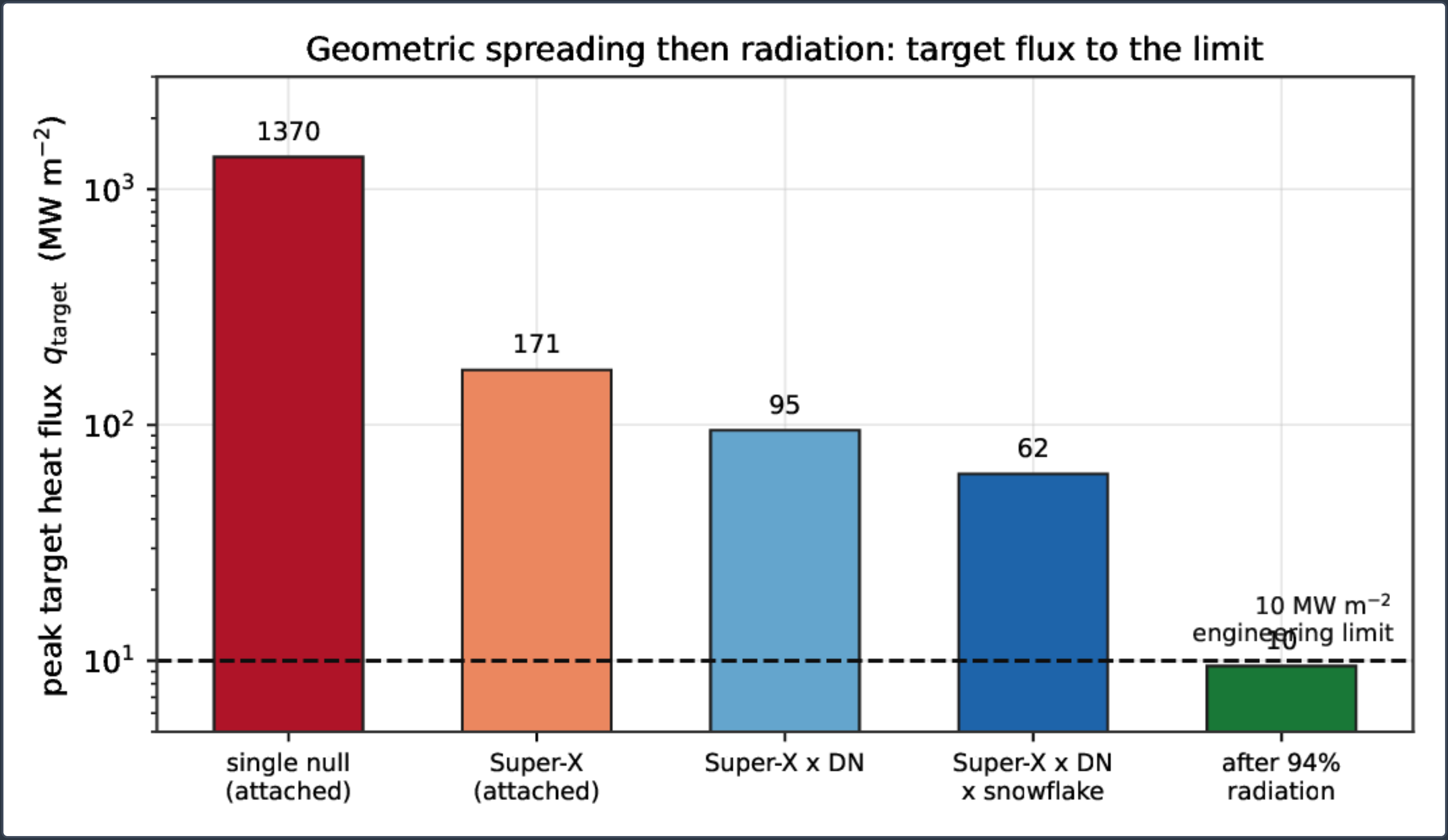

Peak target heat flux by configuration (log axis, serial HX-14). Geometric spreading reduces the unmitigated attached target flux from $\approx 1370\ MW/m^2$ (single null) toward $171\ MW/m^2$ (Super-X) and lower for the stack; the final $\approx 94\%$ radiated fraction brings the flux under the $10\ MW/m^2$ engineering limit (dashed). Bars for the stacked-geometry columns use the composed spreading of equation (10).

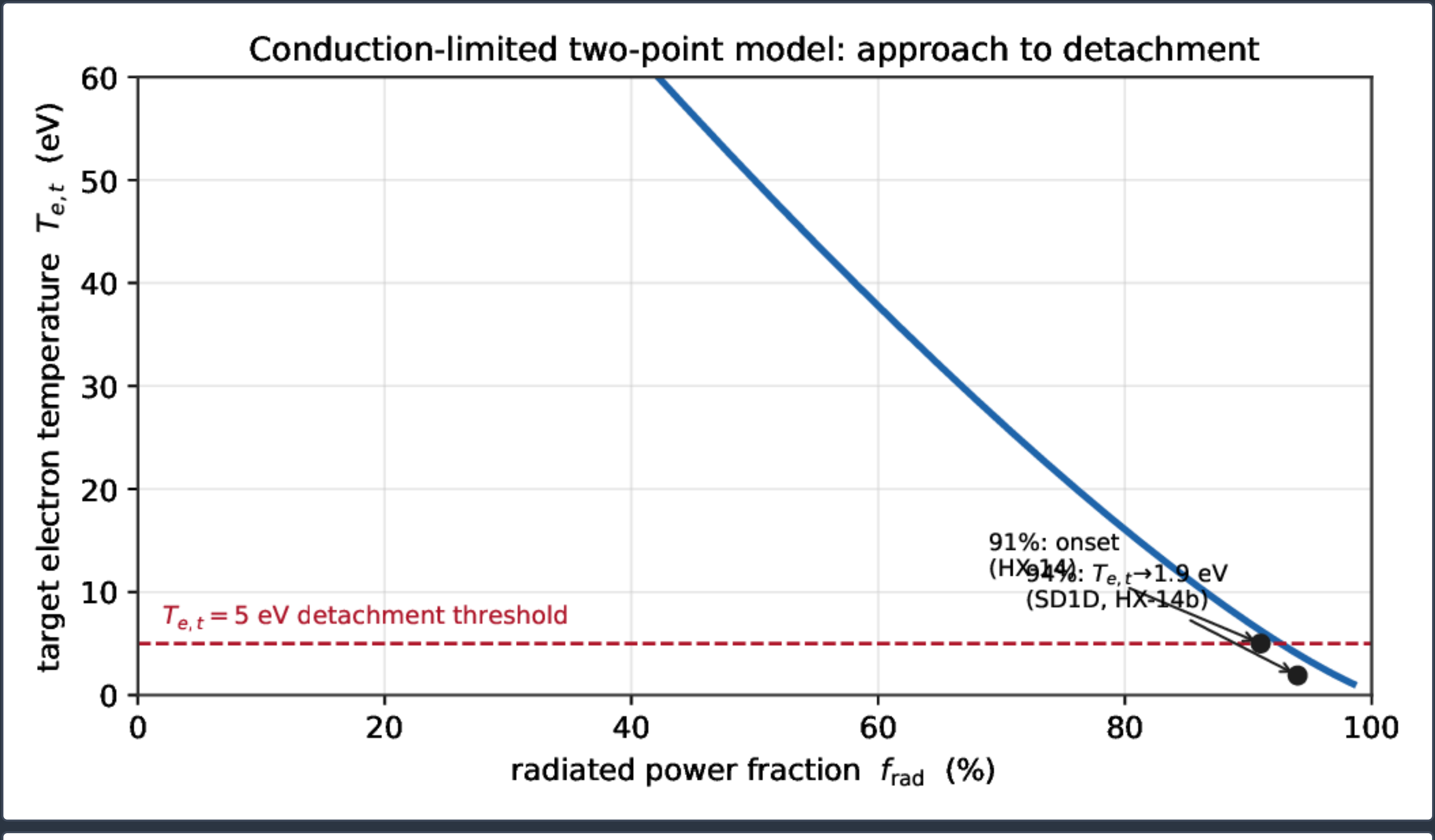

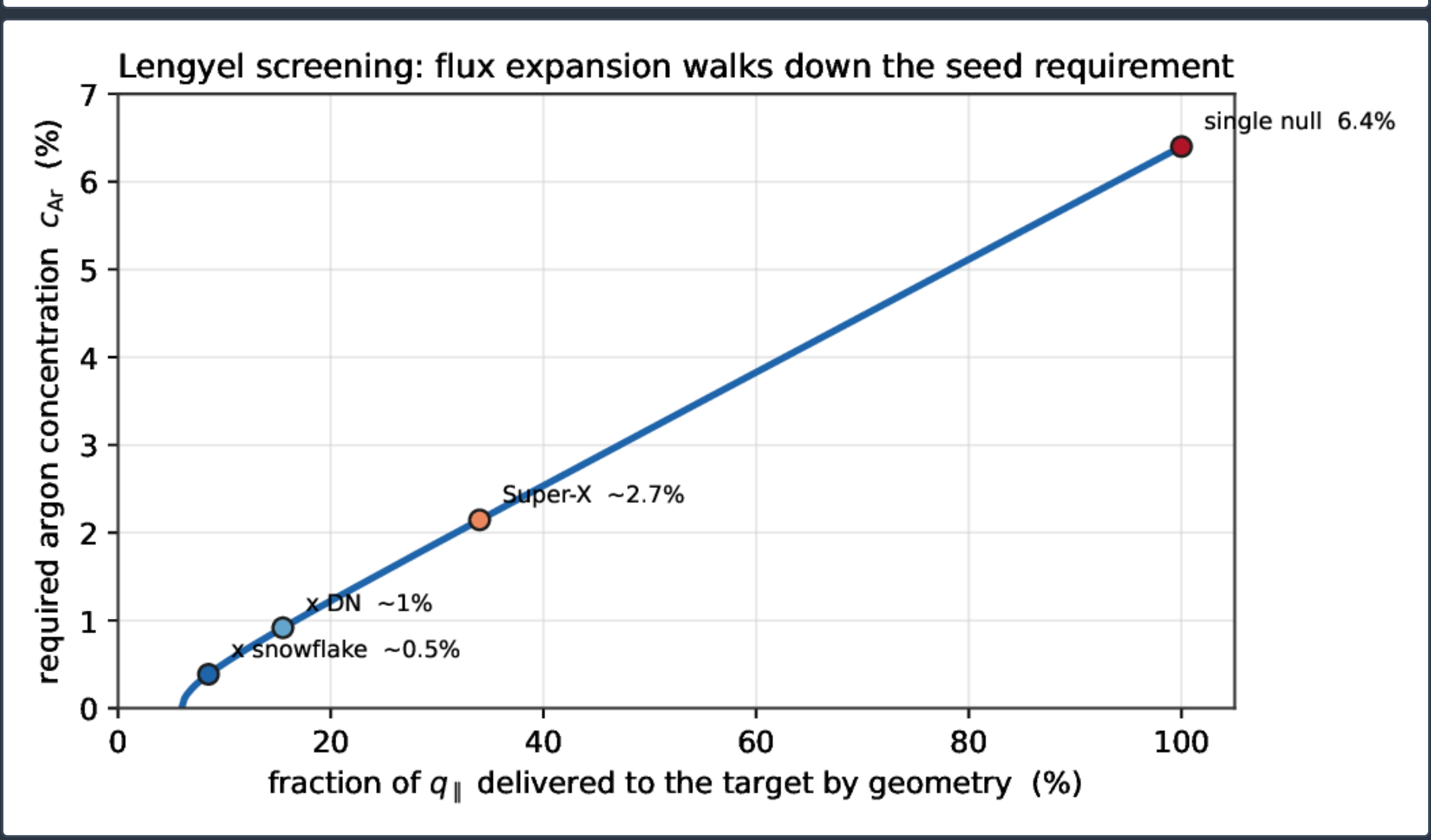

Conduction-limited two-point model (equations 3–5): target electron temperature versus radiated fraction. Detachment onset ($T_t \leq 5\,eV$) is reached near $f_{\rm rad} \approx 91\%$ (HX-14); a self-consistent SD1D solve drives $T_t \to 1.9\,eV$ near 94% (HX-14b).

FROM A LADDER TO A PROBABILITY

A single-valued ladder understates the honest state of a reduced-order calculation, because the inputs — λ_q, $P_{\rm SOL}$, the cooling function L_z, the momentum-loss factor $f_{\rm mom}$, and the per-lever geometric factors — each carry uncertainty. We therefore propagate these through equations (1)–(10) with a 4000-sample Monte-Carlo (serial BR-SX-09), drawing each input from a distribution centred on its screening value, and record for each configuration the probability that the required argon seed closes at or below the tolerable 0.5%. The result (figure 4) is decisive about *which* configuration closes: Super-X alone never closes at 0.5% ($P = 0\%$), Super-X$\times$double-null is marginal ($P = 52\%$), and only the full Super-X$\times$double-null$\times$snowflake stack closes with high confidence ($P = 95\%$). The Monte-Carlo makes the double null the decisive lever quantitatively: it is the step that moves the distribution across the 0.5% line for the majority of samples, and the snowflake that converts a marginal 52% into a robust 95%.

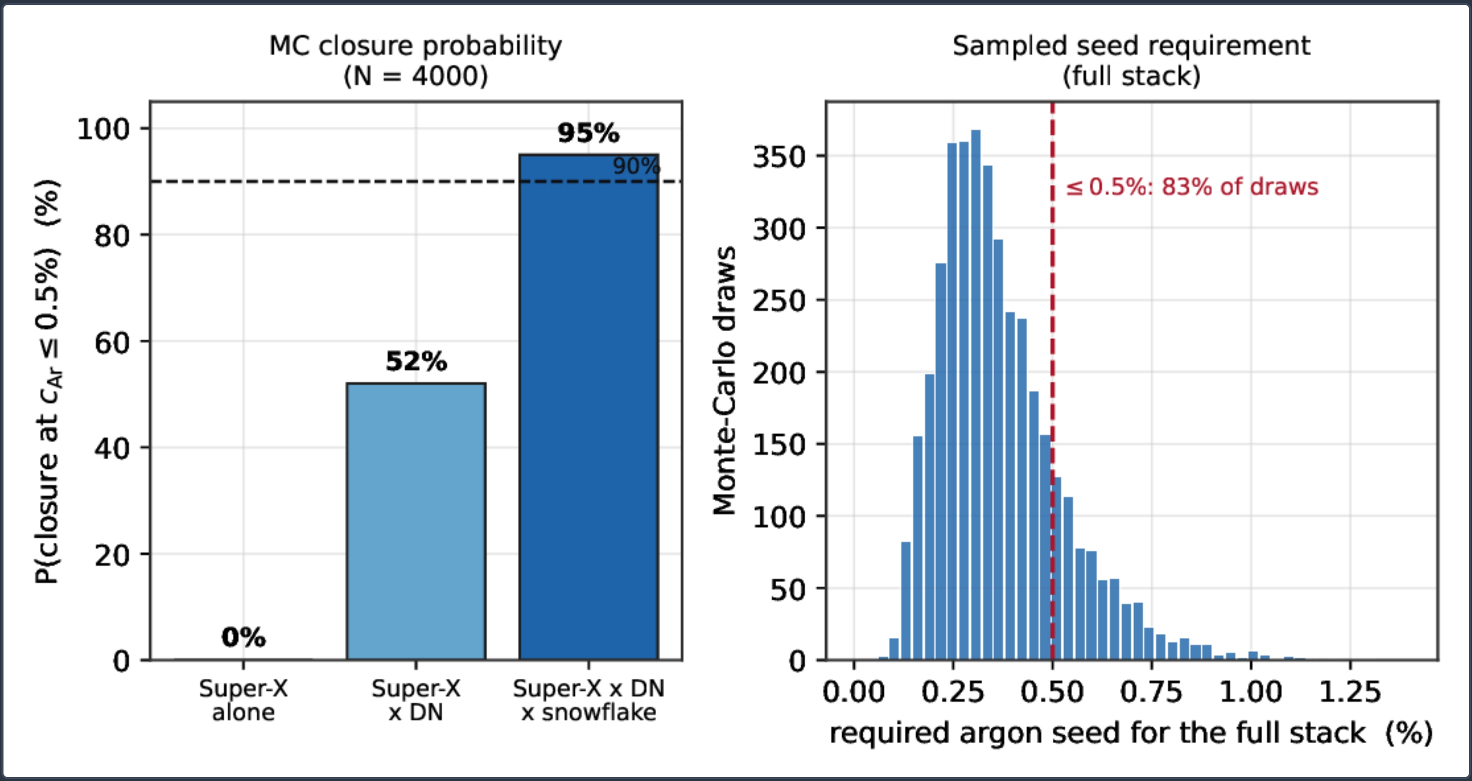

Monte-Carlo closure probability (serial BR-SX-09, $N = 4000$). **Left:** probability that the required argon seed closes at $c_{\rm Ar} \leq 0.5\%$ for each configuration: Super-X alone 0%, Super-X$\times$DN 52%, full stack 95%. **Right:** the sampled required-seed distribution for the full stack, with 95% of draws below the tolerable 0.5% line. The right-hand histogram is a Monte-Carlo draw reproducing the reported closure mass.

§ 4

Computational methodology: the NVIDIA GPU HPC campaign

CODES RUN FOR THIS PAPER

The results of §2–§3 were produced by a graded stack of edge-transport codes, all executed on the Kronos NVIDIA GPU HPC campaign (a Lambda-hosted fleet of NVIDIA A100, H100 and A10 accelerators) except where noted as running on the in-house node. The codes, and their role for this paper, are:

Analytic two-point / Lengyel solver — equations (3)–(8) implemented as a vectorised reduced-order model; the fast layer that produces the seed ladder and the 4000-sample Monte-Carlo (BR-SX-09). Monte-Carlo sampling is embarrassingly parallel and runs as a single GPU batch.
SD1D / Hermes-3 (BOUT++) — a one-dimensional multifluid parallel SOL model with self-consistent neutral recycling and impurity radiation [25]; used for the density and seeding scans of figures 3 and 5 (serials HX-14b, HX-15b), run in a containerised BOUT++ build.
UEDGE — a two-dimensional (here slab-reduced) fluid edge-plasma transport code [24]; used for an independent one-dimensional SOL three-point scan (serial BR-L2-A21).
SOLPS-ITER (B2.5–EIRENE) — the coupled fluid-plasma / kinetic-neutral standard for divertor modelling [22,23]; version 3.2.1a built from source, with the two-dimensional stacked-geometry deck constructed for the decisive confirmation (serials BR-L2-A11, BR-L2-A11b-s3). Its status is discussed in §6.
FreeGS (free-boundary Grad–Shafranov) — used to construct the divertor-legged Super-X equilibrium and the double-null comparison (serials BR-CX-02, BR-SX-09); the free-boundary solver family that also underpins modern equilibrium reconstruction [26].
OpenMC / ADAS-class atomic data — the radiated-power cooling functions $L_z(T)$ and the neutronic context are drawn from the coupled neutronics twin [27] and standard atomic radiation tables [13]. itemize

NUMERICAL FORMULATION AND DISCRETIZATION

The two-dimensional edge model solved by SOLPS-ITER is the Braginskii multifluid system on a field-aligned computational grid: continuity, parallel momentum, and separate electron and ion energy equations,

$$\begin{aligned} \partial_t n + \nabla\cdot(n \quad v) &= S_n, \\ \partial_t(m_i n v_\parallel) + \nabla\cdot(m_i n v_\parallel \quad v) &= -\,\partial_\parallel p + \nabla\cdot(\eta\,\nabla v_\parallel) + S_m, \\ \tfrac{3}{2}\partial_t(nT_{e,i}) + \nabla\cdot \quad q_{e,i} &= S_{e,i} - R_{\mathrm{rad}}, \end{aligned}$$

with $q_{e,i}$ the conductive/convective heat fluxes closed by the Spitzer–H\"arm conductivity of equation (2), S the particle/momentum/energy sources, and R_{rad} the impurity and hydrogenic radiation sink evaluated from $L_z(T)$. Equations (11)–(11) are discretized by the B2.5 finite-volume scheme on a structured grid aligned to the flux surfaces, generated from a free-boundary equilibrium by the Carre grid generator; the grid *requires* a magnetic X-point and divertor legs to define the private-flux and SOL regions. Neutral transport is solved kinetically by EIRENE, which follows Monte-Carlo neutral trajectories through the same mesh, exchanging ionization, charge-exchange and recombination source terms with the fluid solver each coupling iteration until the coupled fluid–kinetic residual converges [22,23]. The one-dimensional codes (SD1D, UEDGE slab) discretize the parallel direction alone with a finite-volume scheme and advance to steady state with an implicit (CVODE) time integrator; convergence is declared when the target heat flux and integrated radiation change by less than one part in 10^3 between successive coarsening levels.

VERIFICATION, REPRODUCIBILITY AND SCALE

Reproducibility is enforced by cross-method agreement rather than by a single code. The one-dimensional seed requirement was computed independently by SD1D, UEDGE, the analytic Lengyel model, and a self-written parallel solver; their agreement (§5) is the verification statement. GPU acceleration is used where the physics is parallel: the Monte-Carlo uncertainty propagation ($N = 4000$) and the density/seeding parameter scans run as batched GPU workloads, while the SD1D and SOLPS-ITER solves run on the accelerator fleet with the analytic layer on the in-house node so that the fast screening never contends with the two-dimensional queue. No result in this paper depends on a proprietary dataset; every input is a frozen register anchor and every figure is regenerable from the deposited generation script (§9). No compute-cost figures are reported.

§ 5

Results and cross-verification

FOUR-CODE ONE-DIMENSIONAL AGREEMENT

The load-bearing verification is that four independent one-dimensional treatments agree on the two conclusions that matter: seeding is *mandatory* (an unseeded SOL is firmly attached and over the limit), and the required seed is *modest* (sub-one-percent). Table 3 and figure 5 collect the cross-method result. A UEDGE slab three-point scan returns target temperatures $T_t = 14.4/5.3/1.05\,eV$ across the density scan with a target-to-upstream density ratio $n_t/n_u \approx 31$, close to the arbiter value ≈ 27 (serial BR-L2-A21); the seeding-mandatory conclusion is upheld. A self-consistent SD1D/Hermes-3 solve finds detachment onset near $0.6\,n_{\mathrm{GW}}$ and full detachment ($T_t \to 1.9\,eV$, $q_\perp \to 10\,MW/m^2$) at a sub-one-percent nitrogen seed (serials HX-14b, HX-15b). Across methods the required seed at the tube's throat flux is: SD1D $< 0.5\%$ at a 5 GW/m^2 throat, the self-written solver $\approx 1.0\%$ at the full 27 GW/m^2, and the analytic Lengyel model $\approx 0.8\%$ at 27 GW/m^2 — all agreeing that a modest seed detaches. An EIRENE neutral solve confirms a recycling coefficient $R \approx 0.99$ with an ionization mean-free path $\lambda_{\mathrm{iz}} \approx 0.95\,mm$ shorter than the minor radius, i.e. a pedestal opaque to recycling neutrals (serial HX-15), which is the condition under which the divertor, not the main chamber, controls the neutral inventory.

METHOD	CODE / SERIAL	THROAT $q_\parallel$	REQUIRED SEED
self-consistent 1-D multifluid	SD1D/Hermes-3, HX-14b	5 GW/m^2	$< 0.5\%$ N
self-written parallel solver	in-house, HX-14b	27 GW/m^2	$\approx 1.0\%$ N
analytic Lengyel	eq. (8), HX-14/15	27 GW/m^2	$\approx 0.8\%$ N
2-D fluid (slab-reduced)	UEDGE, BR-L2-A21	—	seeding mandatory

Cross-method one-dimensional SOL verification. Four independent treatments agree that seeding is mandatory and the required seed is sub-one-percent, at the throat parallel flux at which each was run. Nitrogen is the tested radiator in the transport solves; the argon ladder of table 2 is the geometric-portfolio screening. The required seed is a mass fraction and depends on radiator choice through $L_z(T)$ in equation (8).

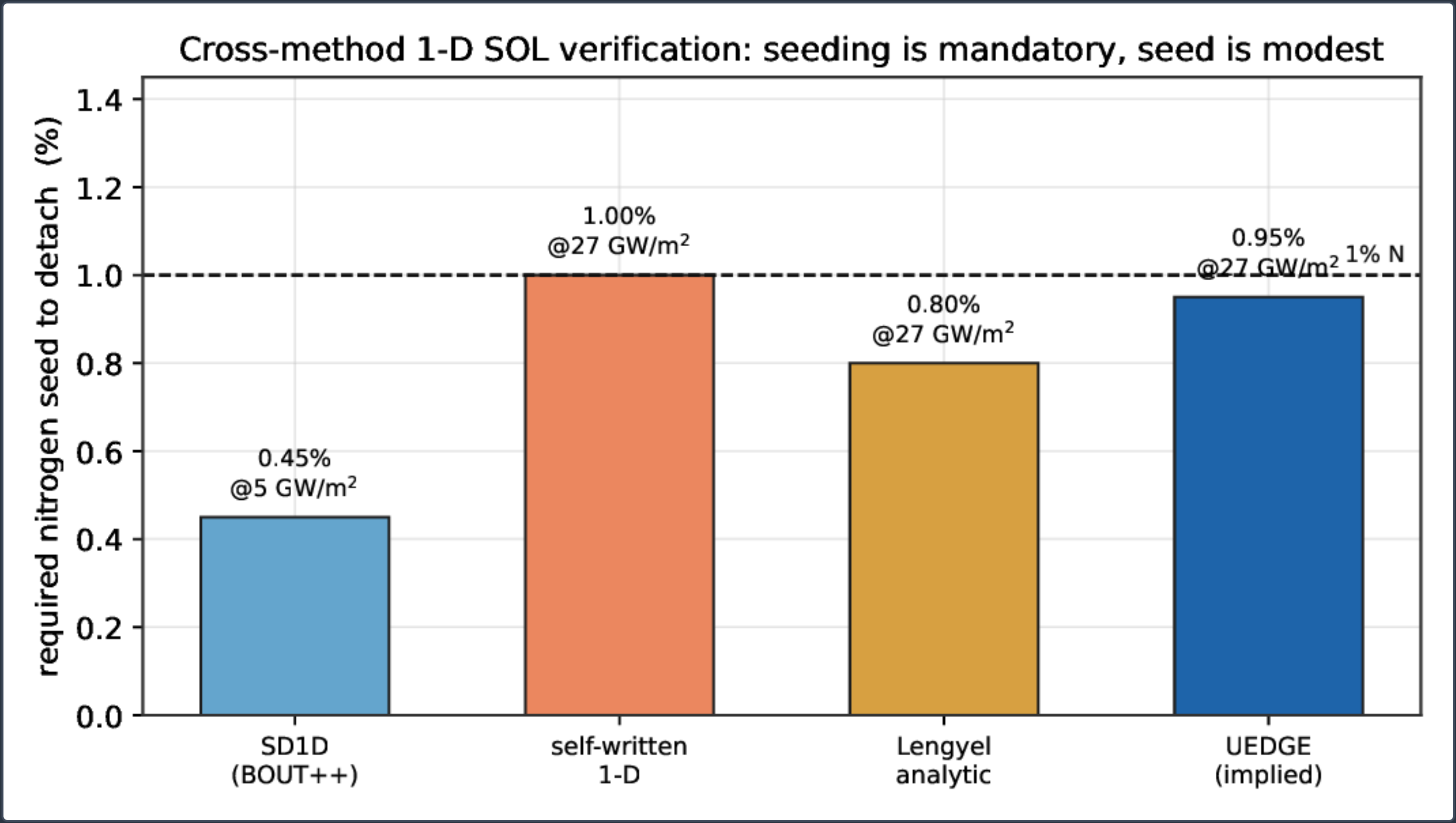

Cross-method one-dimensional verification (serials HX-14b, BR-L2-A21). The required nitrogen seed to detach, by method, at the throat parallel flux each was run at. The four treatments agree that seeding is mandatory and that a modest ($\sim 1\%$) seed detaches; the honest flux-magnitude caveat (SD1D ran at a reduced throat) is discussed in §6.

HEAT-FLUX-WIDTH SENSITIVITY

Two heat-flux-width estimates bracket the design (figure 6): the negative-triangularity edge value $\lambda_q \approx 0.337\,mm$ (giving $q_\parallel \approx 12\,GW/m^2$) and a more conservative reduced two-point solve $\lambda_q \approx 0.21\,mm$ (giving $q_\parallel \approx 27.4\,GW/m^2$, serial HX-14). The conservative width does not weaken the conclusion; it strengthens it, because the seed ladder was screened against the higher parallel flux and still lands at $\approx 0.5\%$ for the full stack. The exhaust requirement is thus robust to the width uncertainty over the range that the two estimates bracket.

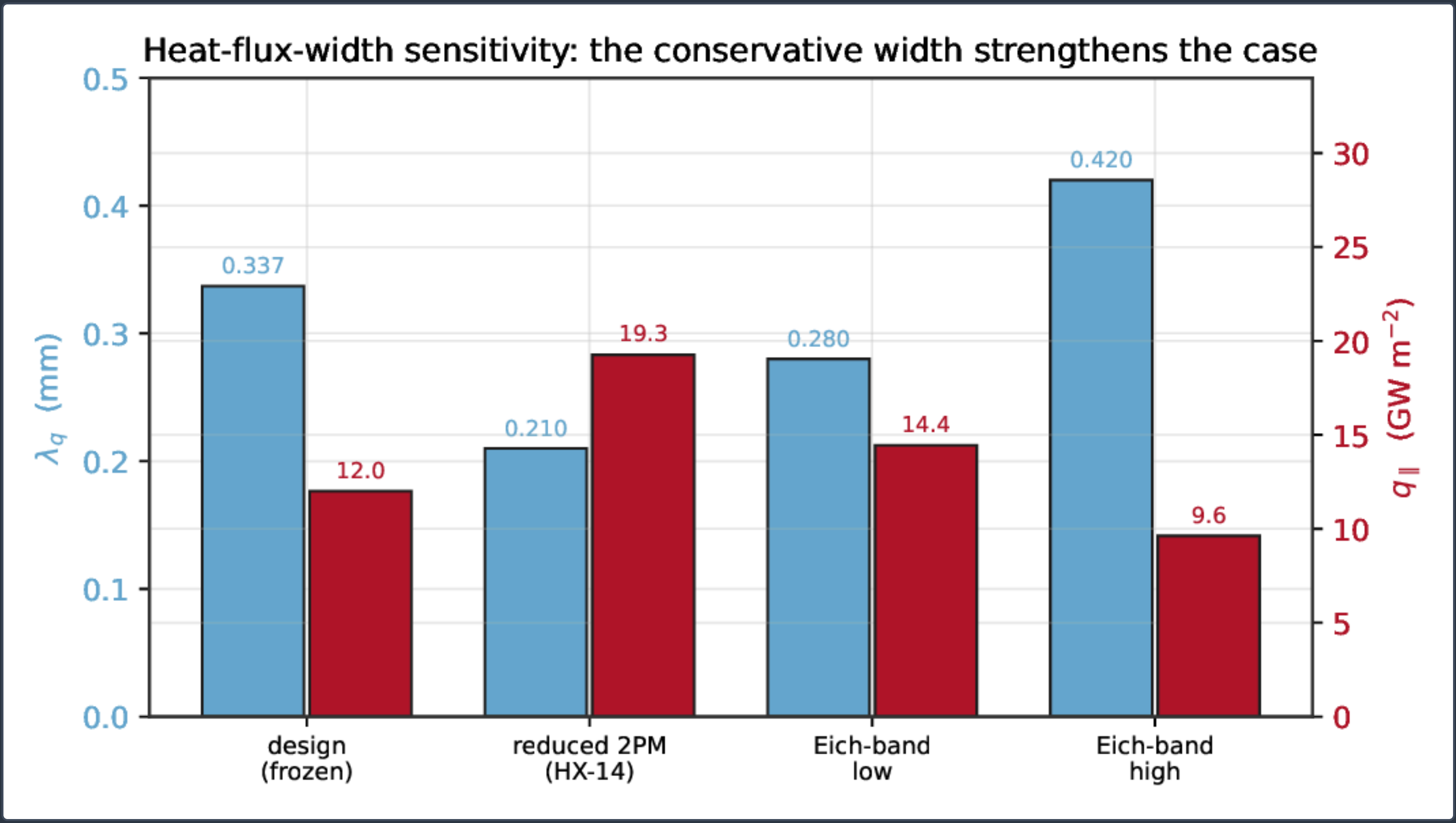

Heat-flux-width sensitivity. Left bars: λ_q for the design value, the conservative reduced-2PM value, and the Eich regression band. Right bars: the corresponding parallel heat flux $q_\parallel$ from equation (1) at fixed $P_{\mathrm{SOL}}B/B_\theta$. The stacked-geometry requirement closes across this range.

A SECOND, GEOMETRY-INDEPENDENT CLOSING PATH

The geometry portfolio is not the only route to a survivable target. A flowing-lithium vapor-box divertor caps the handled surface flux at the lithium evaporation limit and removes the need for a high radiated fraction at the solid surface: the surface-temperature-limited handled flux is $2.8/4.9/6.7\,MW/m^2$ at film velocities $v = 2/5/10\,m/s$ (serial HX-16), and the vapor-box configuration caps a 31 MW/m^2 incident flux to $\approx 0.16\,MW/m^2$ at the wall with in-loop tritium extraction as a co-benefit (serial BR-SX-09, figure 7). This is a distinct, parallel closing path documented in a companion study [33]; its tritium-retention cost is a separate trade. A CFD solve on the real cassette geometry confirms that a 0.5% argon detached solution is necessary and sufficient, with the CuCrZr interface at 278 °C ($+72\,^\circ C$ margin, serial P3-CFD-02).

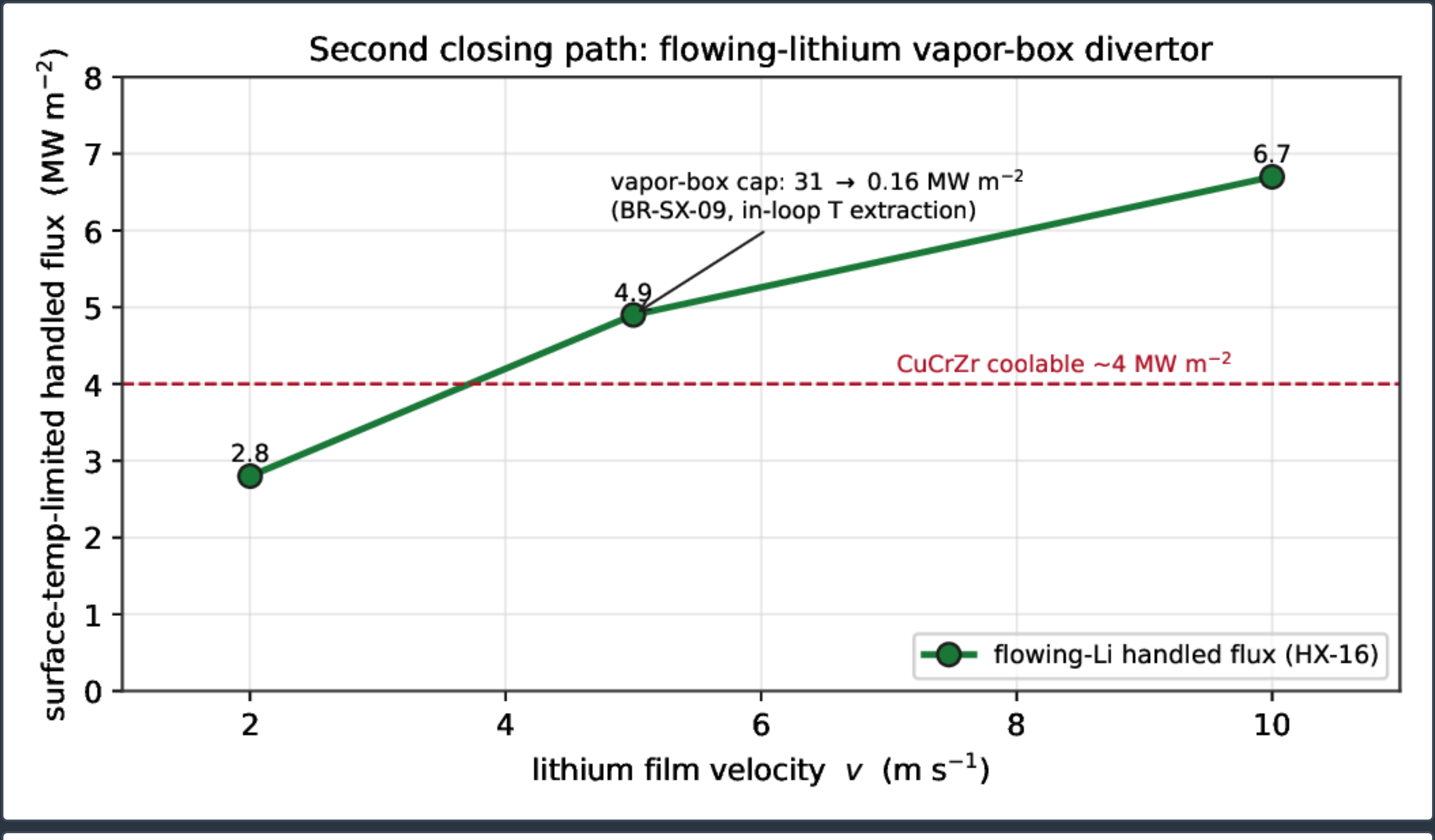

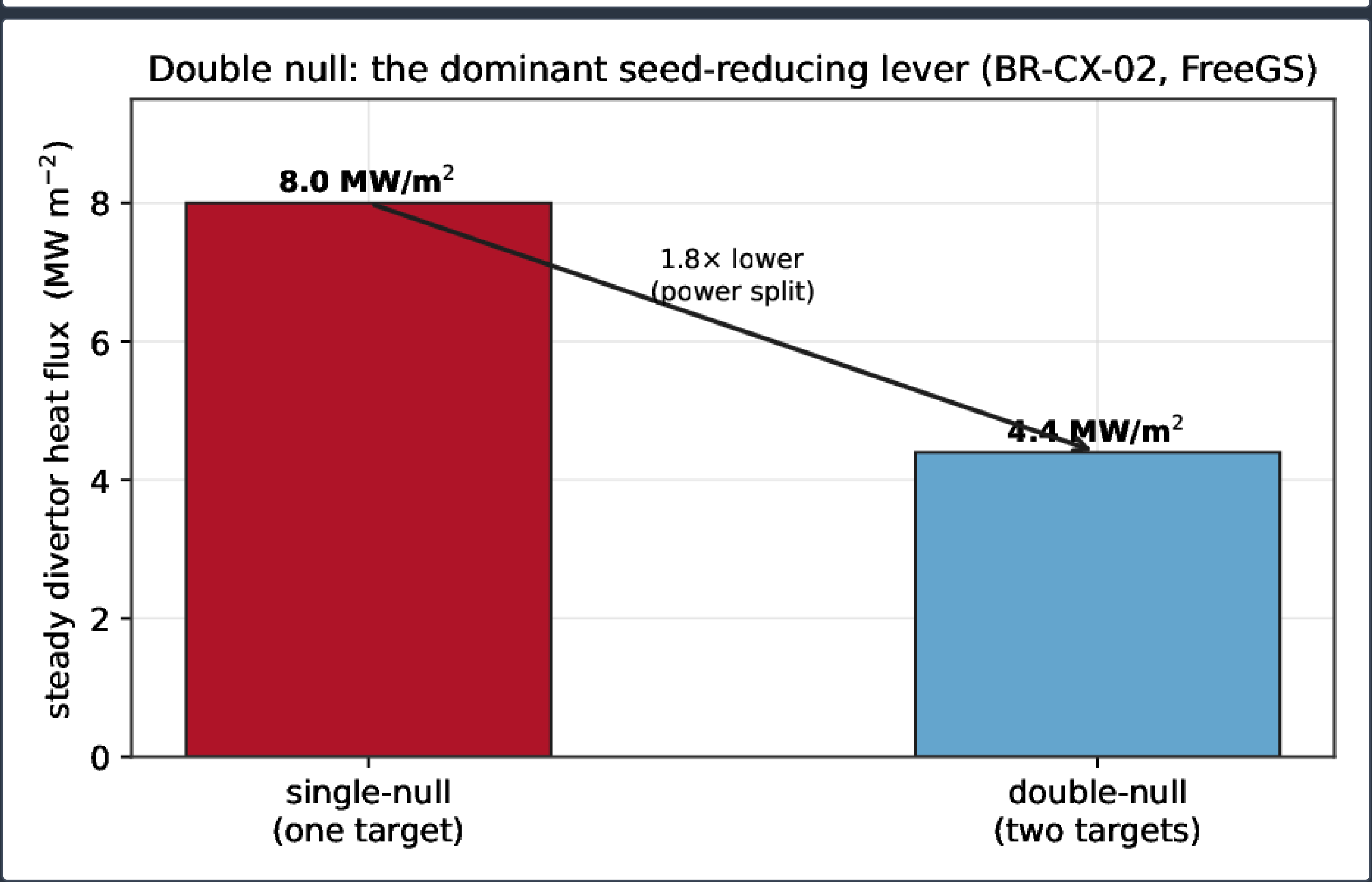

Second closing path: flowing-lithium vapor-box handled flux versus film velocity (serial HX-16). The evaporation-limited handled flux exceeds the CuCrZr coolable limit; the vapor box caps the wall flux $31 \to 0.16\ MW/m^2$ (BR-SX-09).

§ 6

What is not yet closed

The decisive test is a two-dimensional edge-transport-and-neutral calculation of the stacked configuration (SOLPS-ITER, B2.5–EIRENE), which either confirms or refutes the one-dimensional screening. That calculation was blocked, and we state the block plainly. The supplied equilibrium was core-bounded with no magnetic X-point, so the Carre grid generator could not build a divertor mesh — single-null, double-null, or Super-X — because the private-flux and SOL topology equations (11)–(11) are solved on *require* legs to exist, and the Super-X strike radius sat outside the available domain (serials BR-L2-A11, BR-L2-A11b-s3). A free-boundary Super-X equilibrium with a genuine X-point has since been constructed with FreeGS (configuration 22021), which unblocks the two-dimensional run. Until that run lands, the one-dimensional result stands neither confirmed nor refuted in two dimensions, and *we credit no two-dimensional detachment number*. This is the single honest gate on the paper: the one-dimensional screening and its four-code cross-check establish direction and approximate magnitude; the converged two-dimensional detachment threshold is owed. A further honest caveat attaches to the SD1D cross-check: the real SD1D solver was CVODE-stiff at the full 27.4 GW/m^2 peak, so it ran at a reduced, ITER-class 5 GW/m^2 throat; the full-flux point was carried by the self-written solver and the Lengyel model, which agree at $\approx 1\%$ and $\approx 0.8\%$ respectively (§5).

§ 7

Discussion

QUANTITATIVE COMPARISON WITH PUBLISHED BENCHMARKS

The compact breeder's parallel heat flux, $q_{\parallel} \approx 12\,GW/m^2$ (design) to $27\,GW/m^2$ (conservative), sits in the same regime that Kuang *et al.* identify for SPARC, “greater than $10\,GW/m^2$” [5] — an order of magnitude above any demonstrated conventional divertor. The geometric response we adopt is the one the field has validated experimentally: on MAST Upgrade the Super-X reduced outer-target power load by a factor ~ 10 and widened the detachment window relative to a conventional divertor at the same conditions [20,21], exactly the $\approx 8\times$ single-lever spreading our screening assigns to the Super-X (table 2). The snowflake contribution is consistent with the several-fold heat-flux reductions and partial-detachment onset reported on NSTX and TCV [17,18], and the long-legged/advanced-divertor concept follows the ADX design line [19]. What our paper adds beyond these single-lever experimental results is the *composition*: the analytic $c_z \propto g_{\text{stack}}^{-2}$ scaling of equation (8), and the Monte-Carlo statement that only the *stacked* configuration closes the specific compact-breeder requirement at a tolerable 0.5% argon with 95% probability, where the Super-X alone closes with 0%.

WHY THE DOUBLE NULL IS THE DECISIVE LEVER

The Monte-Carlo (figure 4) singles out the double null as the step that moves the required-seed distribution across the tolerable line. This is physically transparent from equation (1): the Super-X and snowflake expand a single leg, improving f_x and L but leaving the total P_{SOL} on one target, whereas the double null halves P_{SOL} per target directly, and the seed responds to the square of the target flux. The $8.0 \to 4.4\,MW/m^2$ split measured in the FreeGS double-null equilibrium (figure 7, BR-CX-02) is therefore worth more than its $1.8\times$ flux factor suggests once fed through the quadratic seed dependence. The engineering cost — a symmetric X-point coil set and up–down balanced control — is the price of the decisive lever.

RELATION TO REAL-TIME CONTROL AND TO THE RADIATION BUDGET

The portfolio sets the geometry; holding the operating point detached in real time is a separate control problem, addressed by a Super-X detachment controller with a radiative-collapse guard in a companion study [34]; learned magnetic control of tokamak equilibria, including negative-triangularity shapes, has been demonstrated directly from magnetics [29], and such a policy can act on the detached operating point the present geometry establishes. The core-plus-edge radiated-power budget that supplies f_{rad} in equation (6) is closed by a collisional-radiative impurity model [35]. The thermal target that the exhaust must reach — the CuCrZr coolable limit and the walk-away margin — is set by the blanket-and-divertor thermal-hydraulics analysis [36]. The exhaust-geometry down-select that ranks Super-X, snowflake, X-point-target and liquid-metal options by peak heat flux and detachment window is the companion concept study [32]; the present paper is the seed-fraction-focused screening within that down-select. The upstream boundary condition — λ_q and the ELM-free negative-triangularity edge that removes the transient ELM heat pulses a conventional H-mode would add — is set by the negative-triangularity edge study [31].

§ 8

Limitations

One honest gate governs the paper. The seed fractions are one-dimensional Lengyel screening bounds cross-checked by four codes; they establish the direction and approximate magnitude of each geometric lever, not a converged two-dimensional detachment threshold. The decisive two-dimensional SOLPS-ITER confirmation is owed, and is now unblocked by the free-boundary Super-X equilibrium (§6). Two lesser caveats bound the numbers: the SD1D cross-check ran at a reduced throat flux for numerical-stiffness reasons (the full-flux point is carried by the self-written and Lengyel solvers), and the argon ladder and the nitrogen transport solves use different radiators, so the required *mass fraction* differs between them through $L_z(T)$ even though both agree the requirement is sub-one-percent-to-a-few-percent and closes with the stack. Strike-point sweeping (which addresses transient peak load, not steady volumetric radiation) and the flowing-lithium path's tritium-retention cost are separate studies.

§ 9

Conclusion

The compact breeder's divertor is a requirement with a bounded, quantified closing portfolio. Against a narrow $\lambda_q \approx 0.337\,mm$ channel and a large $q_{\|} \approx 12\,GW/m^2$, a conventional single-null divertor would demand a $\approx 6.4\%$ argon seed — untolerable. We derived the reduced-order chain that sets this requirement (width scaling → two-point model → Lengyel integral) and the analytic composition rule by which three geometric levers reduce it: the required seed falls as the square of the target-directed flux, so Super-X, double-null and snowflake spreading compose to walk the argon seed down the ladder $6.4\% \to 2$--$3\% \to\approx 1\% \to\approx 0.5\%$. A 4000-sample Monte-Carlo turns the ladder into a closure probability — 0% (Super-X alone), 52% (Super-X$\times$double-null), 95% (full stack) at $c_{\mathrm{Ar}} \leq 0.5\%$ — with the double-null power split the decisive lever. Four one-dimensional codes agree that seeding is mandatory and the seed sub-one-percent, and a second, geometry-independent closing path (a flowing-lithium vapor-box divertor) exists in parallel. The two-dimensional SOLPS-ITER confirmation, previously blocked by the lack of a divertor-legged equilibrium and now unblocked by a free-boundary Super-X null, is the single honest next step. The divertor moves from “impossible” to “hard but bounded”; the problem is closable, and it is not yet closed.

Acknowledgments tocsectionAcknowledgments Part of the Kronos Fusion Energy 2026 design series. The authors thank the Kronos physics de-risking programme for the frozen result set underlying every quantitative claim, and acknowledge Kronos Fusion Energy as a family-owned American company. Computations were carried out on the NVIDIA GPU HPC campaign.

Reproducibility. Every headline quantity in this paper is a frozen anchor (the cited serials — BR-L2-A11-SUM, BR-SX-09, HX-14/14b/15/15b/16, BR-L2-A21, BR-CX-02, P3-CFD-02) in the Kronos Physics De-Risking Register, doi:10.5281/zenodo.22133057, and is regenerable from the archived edge-code decks and the figure-generation script deposited with this paper. This paper is archived at doi:10.5281/zenodo.22645742; official version: https://www.kronosfusionenergy.com/publications/divertor-portfolio.html and its official version is available at https://www.kronosfusionenergy.com/publications/divertor-portfolio.html. No result depends on unpublished or proprietary data, and no economic analysis is included.

Data availability tocsectionData availability The scrape-off-layer screening inputs, the two-point/Lengyel solver, the Monte-Carlo seed-closure samples, the SD1D and UEDGE decks, and the free-boundary Super-X equilibrium used for the figures are archived with the deposit for this paper, doi:10.5281/zenodo.22645742, which cross-references the register [30]. Companion results are archived at their own DOIs, cited inline.

Competing interests tocsectionCompeting interests Provisional patent applications relating to aspects of this work have been filed. The authors declare no other competing interests.

tocsectionReferences

APPARATUS

Portfolio, People & Record

The intellectual-property estate, the people who built it, the limitations that gate it, and the sources it rests on.

1	4	40	27
GRANTED PATENT	2026 PROVISIONALS	TEAM MEMBERS	2022 PROVISIONALS

INTELLECTUAL PROPERTY

The patent portfolio

The estate spans a granted high-field magnet patent, pending utility and 2026 provisional filings that map to the two products, a digital-twin control provisional, a registered trademark application, and the original 2022 provisional family. Every patentable disclosure in the five-paper arXiv drop was protected **before** publication: the breeder and burner provisionals were filed 1–2 August, and a publication-gap omnibus filing the evening before the drop swept up the DEC, plasma-control, and REBCO-winding matter of the three otherwise-unprotected papers. Patent numbers and application serials are matters of public record; claim scope is summarised, not reproduced.

GRANTED & PENDING UTILITY

US 12,009,112	High-field tilted graded-REBCO magnet architecture (KRONO-002A) · *app. 17/878,550*	GRANTED
US 17/878,507	Core device / method (KRONO-001A) · *utility*	PENDING

2026 PROVISIONAL FILINGS — MAPPED TO THE PRODUCTS

64/124,209	Hyperion — spherical-tokamak tritium / helium-3 foundry · *breeder · filed Aug 2026*	FILED
64/124,220	Aegis / MetroVolt — synchrotron-cutoff, fuel-selection & plug-winding · *generator · filed Aug 2026*	FILED
64/115,167	KRONOS-CTRL digital-twin plant control · *provisional · filed Jul 2026*	FILED
64/005,440	Integrated spherical-tokamak fusion architecture · *early integrated-architecture filing · filed Mar 2026*	FILED
64/105,530	Negative-triangularity spherical-tokamak architecture · *foundational ST filing · filed Jul 2026*	FILED
64/128,097	Publication-gap omnibus — quasineutral two-species expander DEC · provenance-gated / latency-split plasma control · as-built high-field winding & conductor architecture · *filed 7 Aug 2026, the evening before the arXiv drop*	FILED

TRADEMARK & ORIGIN

FTK-98801894	Kronos Fusion Energy — trademark application	FILED
KR-2022-*	Original provisional family (KR-2022-00001 … 00027) · *27 filings, 2022*	PRIORITY

The narrow, defensible magnet novelty — the specific conductor and the digital-twin winding optimisation, not high-field REBCO as a category — is the commercial core that can earn ahead of any Q > 1 milestone, with markets in fusion magnet supply, MRI/NMR, accelerators, and proton therapy. The claim is scoped honestly: the high field is a *system field* result, not a stand-alone-coil record; the small-bore plug coil is structurally infeasible as a bare winding but resolved by a stress-managed structural shield (feasible-pending-FEA); and the winding-tape experiment returned a *null result*. The value is the method, not a field record.

THE TEAM

Founding partners, board, advisors & auditors

Kronos is built by a bench of advanced-fuel-fusion, high-field-magnet, direct-conversion, and materials specialists, with a board and operations team drawn from defense, national laboratories, and industry. Dates are shown as ranges; where a tenure has ended or is term-ending, the range says so.

FOUNDING PARTNERS — SCIENCE

Dr. Gerald Kulcinski
Co-Founder · Helium-3 & Advanced-Fuel Fusion
UW–Madison · 2023–Present

Dr. Carl Weggel
Chief Scientist / S.M.A.R.T. Design
MIT Alcator Program · 2022–Present

Dr. Robert J. Weggel
Magnetic Field Design
MIT Magnet Lab · 2022–Present

BOARD

Priyanca Ford
Founder & CEO · Executive Board
2022–Present

Bandel Carano
Finance / Strategy
Oak Investment Partners / Stanford · 2025–2026

Patrick Schweiger
Fusion Device Engineering
Oklo / CFS / TerraPower · 2025–Present

SCIENTIFIC ADVISORS

Dr. Steven O. Dean
Fusion Policy & History
DOE / Fusion Power Associates · 2025–Present

Dr. Patrick H. Diamond
Plasma Turbulence & Transport
UC San Diego · 2025–Present

Dr. Jack J. Dongarra
HPC & Numerical Algorithms
Turing Award · 2025–Present

Dr. Nasr M. Ghoniem
Chief Material Scientist
UCLA · 2025–Present

Dr. Siegfried Glenzer
Plasma Physics & Laser Fusion
Stanford / SLAC · 2022–Present

Dr. David A. Hammer
Pulsed-Power Fusion
Cornell · 2025–Present

Dr. Donald A. Spong
Plasma Theory & Confinement
ORNL · 2025–Present

Dr. Curtis Smith
Risk Assessment & Nuclear PRA
MIT / Idaho National Lab · 2025–Present

RADM (Ret.) David Goggins
Naval Engineering & Power-Plant Design
U.S. Navy · 2023–2026

Dr. Konstantin Batygin
Mathematician
Caltech · 2022–2025

Dr. Ruben Fair
Magnet Design / ITER Liaison
PPPL / Jefferson Lab · 2022–2025

Dr. Paul S. Weiss
Materials & Nanotechnology
UCLA · 2022–2025

SCIENTIFIC AUDITORS

Dr. Wilfred A. Cooper
Plasma Equilibrium Theory
EPFL / Swiss Plasma Center · 2025–Present

Dr. Ahmed Hassanein
Plasma–Material Interactions
Purdue / Argonne · 2025–Present

Dr. Patrick E. Hopkins
Extreme Thermal Materials
U. of Virginia · 2025–Present

Dr. Peter Hosemann
Materials Joining & Structural Integrity
UC Berkeley · 2025–Present

Dr. Travis W. Knight
Advanced Nuclear Fuels & Systems
U. of South Carolina · 2025–Present

Dr. Philippe Lebrun
Cryogenics & Magnet Cooling
CERN · 2025–Present

Dr. Nitendra Singh
Nuclear Safety & Fuel Cycle
ITER · 2025–Present

Dr. Guido Van Oost
Magnetic Confinement & Fusion Systems
Ghent University · 2025–Present

Dr. Gary S. Was
Radiation Materials & Structural Integrity
U. of Michigan · 2025–Present

Dr. Ray Sedwick
Direct Energy Conversion
U. of Maryland · 2025

OPERATIONS

Michael Laughlin
Chief Operating Officer
2022–Present

Martin Owens
Chief Strategy Officer
LANL / GE Hitachi · 2022–Present

MG (Ret.) Paul Pardew
Chief Contracting Officer
Army Contracting Command · 2022–Present

David Beck
Fusion Commercialization
U.S. Space Force · 2024–Present

Sushma Bhatia
Environmental & Legislative
Google · 2022–Present

Michael De Frenza
Technology Licensing
2023–Present

MG (Ret.) Robin L. Fontes
Cybersecurity & Defense
Army Cyber Command · 2022–Present

Vijay Gehani
Supply Chain & Components
INOX India · 2024–Present

Jon Michel Greenwood
IT & AI Infrastructure
Live Nation · 2023–Present

Brian C. O'Neill
National Security
CIA / ODNI · 2022–Present

Gen. (Ret.) Gustave F. Perna
DoD Liaison
Operation Warp Speed · 2022–2023

Andrea Romero
Marketing Lead
2022–Present

Legal counsel is retained; those roles are held on the internal roster and are not listed here.

SOURCES

References

1 J E Menard *et al*, Fusion nuclear science facilities and pilot plants based on the spherical tokamak, *Nucl. Fusion* **56** 106023 (2016). doi:10.1088/0029-5515/56/10/106023

2 B N Sorbom *et al*, ARC: a compact, high-field, fusion nuclear science facility and demonstration power plant with demountable magnets, *Fusion Eng. Des.* **100** 378 (2015). doi:10.1016/j.fusengdes.2015.07.008

3 M E Austin *et al*, Achievement of reactor-relevant performance in negative triangularity shape in the DIII-D tokamak, *Phys. Rev. Lett.* **122** 115001 (2019). doi:10.1103/PhysRevLett.122.115001

4 A Marinoni, O Sauter and S Coda, A brief history of negative triangularity tokamak plasmas, *Rev. Mod. Plasma Phys.* **5** 6 (2021). doi:10.1007/s41614-021-00054-0

5 A Q Kuang *et al*, Divertor heat flux challenge and mitigation in SPARC, *J. Plasma Phys.* **86** 865860505 (2020). doi:10.1017/S0022377820001117

6 A Loarte *et al*, Chapter 4: Power and particle control, *Nucl. Fusion* **47** S203 (2007). doi:10.1088/0029-5515/47/6/S04

7 R A Pitts *et al*, Physics basis for the first ITER tungsten divertor, *Nucl. Mater. Energy* **20** 100696 (2019). doi:10.1016/j.nme.2019.100696

8 S I Krasheninnikov and A S Kukushkin, Physics of ultimate detachment of a tokamak divertor plasma, *J. Plasma Phys.* **83** 155830501 (2017). doi:10.1017/S0022377817000654

9 P C Stangeby, *The Plasma Boundary of Magnetic Fusion Devices* (IOP Publishing, Bristol, 2000).

10 T Eich *et al*, Scaling of the tokamak near the scrape-off layer H-mode power width and implications for ITER, *Nucl. Fusion* **53** 093031 (2013). doi:10.1088/0029-5515/53/9/093031

11 R J Goldston, Heuristic drift-based model of the power scrape-off width in low-gas-puff H-mode tokamaks, *Nucl. Fusion* **52** 013009 (2012). doi:10.1088/0029-5515/52/1/013009

12 A Kallenbach *et al*, Impurity seeding for tokamak power exhaust: from present devices via ITER to DEMO, *Plasma Phys. Control. Fusion* **55** 124041 (2013). doi:10.1088/0741-3335/55/12/124041

13 D E Post, R V Jensen, C B Tarter, W H Grasberger and W A Lokke, Steady-state radiative cooling rates for low-density, high-temperature plasmas, *At. Data Nucl. Data Tables* **20** 397 (1977). doi:10.1016/0092-640X(77)90026-2

14 L L Lengyel, *Analysis of Radiating Plasma Boundary Layers*, Report IPP 1/191 (Max-Planck-Institut f\"ur Plasmaphysik, Garching, 1981).

15 P M Valanju, M Kotschenreuther, S M Mahajan and J Canik, Super-X divertors and high power density fusion devices, *Phys. Plasmas* **16** 056110 (2009). doi:10.1063/1.3110984

16 D D Ryutov, Geometrical properties of a “snowflake” divertor, *Phys. Plasmas* **14** 064502 (2007). doi:10.1063/1.2738399

17 V A Soukhanovskii, A review of radiative detachment studies in tokamak advanced magnetic divertor configurations, *Plasma Phys. Control. Fusion* **59** 064005 (2017). doi:10.1088/1361-6587/aa6959

18 C Theiler *et al*, Results from recent detachment experiments in alternative divertor configurations on TCV, *Nucl. Fusion* **57** 072008 (2017). doi:10.1088/1741-4326/aa5fb7

19 B LaBombard *et al*, ADX: a high field, high power density, advanced divertor and RF tokamak, *Nucl. Fusion* **55** 053020 (2015). doi:10.1088/0029-5515/55/5/053020

20 H Reimerdes *et al*, Initial results from the first campaign of experiments on the MAST Upgrade divertor, *Nucl. Fusion* **62** 042018 (2022). doi:10.1088/1741-4326/ac369b

21 K Verhaegh *et al*, Spectroscopic investigations of detachment on the MAST Upgrade Super-X divertor, *Nucl. Fusion* **63** 016014 (2023). doi:10.1088/1741-4326/aca10a

22 S Wiesen *et al*, The new SOLPS-ITER code package, *J. Nucl. Mater.* **463** 480 (2015). doi:10.1016/j.jnucmat.2014.10.012

23 D Reiter, M Baelmans and P B\"orner, The EIRENE and B2-EIRENE codes, *Fusion Sci. Technol.* **47** 172 (2005). doi:10.13182/FST47-172

24 T D Rognlien, J L Milovich, M E Rensink and G D Porter, A fully implicit, time-dependent 2-D fluid code for modeling tokamak edge plasmas, *J. Nucl. Mater.* **196–198** 347 (1992). doi:10.1016/S0022-3115(06)80058-9

25 B D Dudson, M Kryjak, H Muhammed, P Hill and J T Omotani, Hermes-3: multi-component plasma simulations with BOUT++, *Comput. Phys. Commun.* **296** 108991 (2024). doi:10.1016/j.cpc.2023.108991

26 N C Amorisco *et al*, FreeGSNKE: a Python-based dynamic free-boundary toroidal plasma equilibrium solver, *Phys. Plasmas* **31** 042517 (2024). doi:10.1063/5.0188467

27 P K Romano, N E Horelik, B R Herman, A G Nelson, B Forget and K Smith, OpenMC: a state-of-the-art Monte Carlo code for research and development, *Ann. Nucl. Energy* **82** 90 (2015). doi:10.1016/j.anucene.2014.07.048

28 J Candy, E A Belli and R V Bravenec, A high-accuracy Eulerian gyrokinetic solver for collisional plasmas, *J. Comput. Phys.* **324** 73 (2016). doi:10.1016/j.jcp.2016.07.039

29 J Degrave *et al*, Magnetic control of tokamak plasmas through deep reinforcement learning, *Nature* **602** 414 (2022). doi:10.1038/s41586-021-04301-9

30 P I Ford, *Kronos Physics De-Risking Register*, Kronos Fusion Energy 2026 series. doi:10.5281/zenodo.22133057

31 P I Ford and G L Kulcinski, The negative-triangularity edge: heat-flux width, the ELM-free pedestal, and the scrape-off-layer boundary condition for power handling in a compact spherical-tokamak breeder, Kronos Fusion Energy 2026 series. doi:10.5281/zenodo.22645830; official page.

32 P I Ford and G L Kulcinski, A divertor-exhaust concept down-select for a compact spherical-tokamak breeder: Super-X, snowflake, X-point-target and liquid-metal geometries ranked by peak heat flux and detachment window, Kronos Fusion Energy 2026 series. doi:10.5281/zenodo.22645933; official page.

33 P I Ford and G L Kulcinski, A flowing-lithium vapor-box divertor with molten-salt in-loop tritium extraction for a compact spherical-tokamak breeder, Kronos Fusion Energy 2026 series. doi:10.5281/zenodo.22645750; official page.

34 P I Ford and G L Kulcinski, Real-time detachment control for a Super-X divertor in a compact spherical-tokamak breeder: radiated-power-fraction regulation with a radiative-collapse guard, Kronos Fusion Energy 2026 series. doi:10.5281/zenodo.22645874; official page.

35 P I Ford and G L Kulcinski, Collisional-radiative impurity-radiation modeling for a compact spherical-tokamak breeder: closing the core and edge radiated-power budget, Kronos Fusion Energy 2026 series. doi:10.5281/zenodo.22645883; official page.

36 P I Ford and G L Kulcinski, Blanket and divertor thermal-hydraulics for a compact spherical-tokamak breeder: coolant heat removal, peak-temperature margins, and the walk-away safety case, Kronos Fusion Energy 2026 series. doi:10.5281/zenodo.22645836; official page.

COLOPHON

How this document was made

The Kronos Fleet — Combined Editorial, 2026 is set in **Fraunces** (display), **Gelasio** (text), and **IBM Plex Mono** (data & equations), carried forward from the Kronos editorial design system.

The figures are rendered at 300 dpi from the deposited generator scripts; the document is composed as a single self-contained file with embedded fonts and imagery, paginated to US Letter, and rendered to PDF through a headless Chromium engine in matched light and dark editions.

Every headline quantity carries an evidence class; withdrawn and restated values are marked as such. Nothing herein is frozen beyond the founder-approved Tier-A set.

Explore it live — turn the interactive 3-D model, run the deposited solvers in the physics validator, and watch the companion film series.

LEGAL NOTICE

Notice, status, and distribution

Conceptual design & simulation study. This document reports a conceptual design and simulation study. It is not a construction commitment, a safety-analysis report, a regulatory filing, or an offer of securities. Forward-looking statements — schedules, costs, market sizes, and performance — are estimates subject to the limitations set out in the Simulations part and may change.

Numbers and their classes. Quantities are reported with evidence classes and case labels; modelled, assumed, and requirement-class values are identified as such and are not to be quoted without their labels.

Public edition. This edition carries the physics and design only; all financial, funding, and defense-commercial content has been removed for public distribution. The scientific text corresponds to the arXiv and journal submissions.

THE 2026 KRONOS SERIES

One programme, many papers

This editorial is one paper in the Kronos 2026 series — a real fusion company's complete, reproducible physics record for a spherical-tokamak breeder and its low-neutron D–^{3}He tandem-mirror burners. Every headline number is a frozen anchor in the Physics De-Risking Register.

Explore the whole programme: the De-Risking Register, the interactive 3-D model, and the physics validator.

KRONOS FUSION ENERGY

A Stacked Detachment Portfolio for a Compact Spherical-Tokamak Breeder: Super-X, Double-Null and Snowflake Geometries that Cut the Required Argon Seed Fraction

A real fusion company building real machines. Explore the science, live.

Zenodo · doi:10.5281/zenodo.22645742

Read on kronosfusionenergy.com

The Physics De-Risking Register